

Comprehensive Investigation of the $\text{Na}_3\text{V}_2(\text{PO}_4)_2\text{F}_3$ – $\text{NaV}_2(\text{PO}_4)_2\text{F}_3$ System by Operando High Resolution Synchrotron X-ray Diffraction

M. Bianchini,^{†,‡,§,⊥} F. Fauth,^{||} N. Brisset,[‡] F. Weill,[‡] E. Suard,[§] C. Masquelier,^{†,⊥,♯} and L. Croguennec^{*‡,⊥,♯}

[†]Laboratoire de Réactivité et de Chimie des Solides, CNRS-UMR#7314, Université de Picardie Jules Verne, F-80039 Amiens Cedex 1, France

[‡]CNRS, Univ. Bordeaux, Bordeaux INP, ICMCB UPR 9048, F-33600 Pessac, France

[§]Institut Laue-Langevin, 71 Avenue des Martyrs, F-38000 Grenoble, France

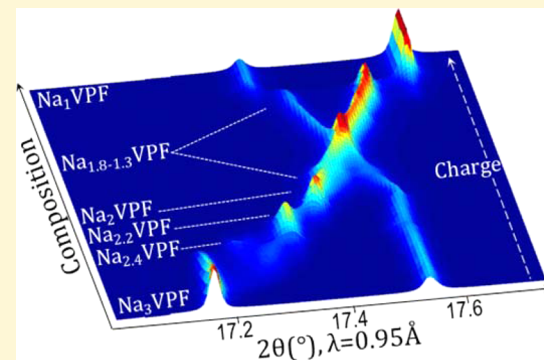
^{||}CELLS - ALBA synchrotron, E-08290 Cerdanyola del Vallès, Barcelona, Spain

[⊥]RS2E, Réseau Français sur le Stockage Electrochimique de l'Energie, FR CNRS 3459, F-80039 Amiens Cedex, France

^{*}ALISTORE-ERI European Research Institute, FR CNRS 3104, F-80039 Amiens Cedex, France

S Supporting Information

ABSTRACT: $\text{Na}_3\text{V}_2(\text{PO}_4)_2\text{F}_3$ is a positive electrode material for Na-ion batteries which is attracting strong interest due to its high capacity, rate capability, and long-term cycling stability. The sodium extraction mechanism from this material has been always described in the literature as a straightforward solid solution, but several hints point toward a more complicated phase diagram. In this work we performed high angular resolution synchrotron radiation diffraction measurements, realized operando on sodium batteries upon charge. We reveal an extremely interesting phase diagram, created by the successive crystallization of four intermediate phases before the end composition $\text{NaV}_2(\text{PO}_4)_2\text{F}_3$ is reached. Only one of these phases undergoes a solid solution reaction, in the interval between 1.8 and 1.3 Na per formula unit. The ability to resolve weak Bragg reflections allowed us to reveal differences in terms of symmetry among the phases, to determine their previously unknown space groups, and to correlate them with sodium (dis)ordering in the structure. Rietveld refinements enabled us to follow fine structural modifications in great detail. Intermediate identified phases are not simply described by their unit cell parameters, but bond-length variations can be tracked, as well as polyhedral distortions and site occupancy factors for mobile sodium ions. For $\text{NaV}_2(\text{PO}_4)_2\text{F}_3$ a full crystal structure determination was also carried out for the first time directly from operando measurements, assigning it to the $\text{Cmc}2_1$ space group and revealing two vanadium environments: V^{3+} and V^{5+} . Our study demonstrates that improved angular resolution and high intensity diffraction data are key parameters for direct observation of fine reaction pathways in electrode materials and that the obtained insight is crucial for the understanding of (de)intercalation mechanisms in Na-ion batteries.



INTRODUCTION

Li-ion is nowadays the technology of choice for portable applications, and it is spreading to the automotive world.¹ However, concerns about the future availability and prize of lithium resources stimulate research to find suitable alternatives to this successful technology.^{2,3} Among many others, Na-ion appears to be the most obvious choice, as it is based on the same fundamental processes of ion intercalation as Li-ion.⁴ Despite several advantages of sodium, including lower price and very high earth-abundance (not to mention positive environmental aspects), important drawbacks must be overcome to ensure a bright future to the Na-ion technology. A less negative standard reduction potential (-2.7 V vs SHE for the $\text{Na}^{+}_{\text{aq}}/\text{Na}$ against -3.04 V for the $\text{Li}^{+}_{\text{aq}}/\text{Li}$ one) and a higher molecular weight both contribute to reduce the energy density, whereas

the larger ionic radius (1.20 Å for Na^{+} against 0.7 Å for Li^{+}) can in principle reduce ions mobility.

Several Na-ion positive electrode materials have been adapted so far from the Li-ion technology: for example, NaCoO_2 ,^{5,6} NaFePO_4 ,^{7–9} and NaVPO_4F .^{10,11} Other interesting structural families include the fast ionic conductors $\text{Na}_3\text{V}_2(\text{PO}_4)_3$ ^{12–16} and $\text{Na}_3\text{V}_2\text{O}_{28}(\text{PO}_4)_2\text{F}_{3-2\delta}$ ^{17–22} for which the “solid solution” is driven by the O/F ratio. The term “solid solution” is put into quotes because this definition applies to a domain where the change in composition induces a continuous modification of the structural parameters but in the same crystallographic structure. However, as discussed in the next

Received: January 28, 2015

Revised: March 29, 2015

Published: March 30, 2015



paragraph, we recently showed that the end member $\text{Na}_3\text{V}_2(\text{PO}_4)_2\text{F}_3$ ($\delta = 0$) is described in the *Amam* orthorhombic space group whereas the end member $\text{Na}_3(\text{VO})_2(\text{PO}_4)_2\text{F}$ ($\delta = 1$) is described in the $P4_2/mnm$ tetragonal space group. Such compositions could solve the problems faced by the Na-ion technology of less negative potential and bigger molecular weight due to the availability of 3 Na^+ ions per formula unit and to the possible oxidation of V^{3+} into V^{4+} and then V^{5+} . For the most interesting composition in terms of energy density, i.e., $\text{Na}_3\text{V}_2(\text{PO}_4)_2\text{F}_3$ ($\delta = 0$), the extraction of 2 Na^+ ions has been experimentally demonstrated following two main voltage–composition plateaus at about 3.7 and 4.2 V vs Na^+/Na , delivering $\sim 507 \text{ Wh/kg}$ (128 Ah/kg at an average potential of 3.95 V). This value is comparable to commercial positive electrodes developed for Li-ion batteries as LiFePO_4 (580 Wh/kg) and LiMn_2O_4 (480 Wh/kg). Figure 1

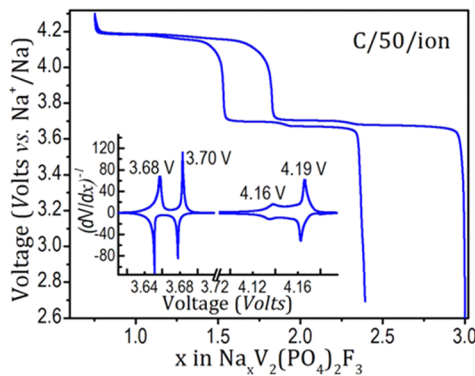


Figure 1. Galvanostatic electrochemical cycling of a $\text{Na}_3\text{V}_2(\text{PO}_4)_2\text{F}_3$ //Na battery at C/50 rate per exchanged ion. Inset: Inverse derivative curve (dV/dx) $^{-1}$ showing the presence of several electrochemical features.

displays a typical galvanostatic voltage–composition electrochemical curve for $\text{Na}_3\text{V}_2(\text{PO}_4)_2\text{F}_3$ vs Na^+/Na . From this figure and from various recent reports it can be noticed that the electrochemical features are actually structured.^{26–28} Indeed, the inverse derivative curve (inset) shows two peaks very close

to each other at 3.68 and 3.70 V vs Na^+/Na for the lowest plateau and two at 4.16 and 4.19 V vs Na^+/Na for the highest one. These are the first hints suggesting a quite complicated phase diagram for this material upon Na^+ extraction. The deintercalation of the third sodium around 5 V could even lead to a huge energy density (>800 Wh/kg), but its achievement is not straightforward because of the high voltage involved, lying outside the stability window of available electrolytes.²⁸ The group of J.B. Goodenough²⁹ recently reported theoretical calculations showing that such a high voltage is due to the strong Coulombic attraction between Na^+ and the polyanions. It was suggested that swapping the O and F anions to the less-electronegative Cl and Br ones could facilitate the extraction.

On the basis of single-crystal and powder X-ray diffraction experiments, the crystal structure of $\text{Na}_3\text{V}_2(\text{PO}_4)_2\text{F}_3$ was thought to be well-established. Le Meins et al.³⁰ initially described it using the tetragonal space group $P4_2/mnm$, with a distribution of Na^+ ions over two sites: a first one, Na1_p , fully occupied, and a second one, Na2_p , half-occupied only (here the subscript helps identify the space group used, since several ones will be encountered in the following). The crystal structure of $\text{Na}_3\text{V}_2(\text{PO}_4)_2\text{F}_3$ highlights pairs of V^{3+} ions localized in bioctahedral environment and surrounded by four oxygen and two fluorine each, these fluorine being along the axis of the biotahedra. These $\text{V}_2\text{O}_8\text{F}_3$ have regular V–O and V–F bond lengths close to 2 Å, and they are bridged by PO_4 tetrahedra, building a 3D framework with large tunnels along the [110] and [1̄10] directions, where sodium ions are placed. The same space group is used to describe the other members of the “solid solution” $\text{Na}_3\text{V}_2\text{O}_{2\delta}(\text{PO}_4)_2\text{F}_{3-2\delta}$. $\text{V}_2\text{O}_8\text{F}_3$ biotahedra become $\text{V}_2\text{O}_{8+2\delta}\text{F}_{3-2\delta}$ with 2δ vanadium ions present as vanadyl $\{\text{VO}\}^{2+}$ and the others ($2-2\delta$) as V^{3+} . Here, along the chains, the V=O vanadyl type bonds are much shorter (≈ 1.6 Å) than V–F ones (≈ 2.1 Å). In our recent work²⁶ we exploited the high angular resolution offered by synchrotron radiation diffraction to reveal a subtle ($b/a = 1.002$) orthorhombic distortion in the stoichiometric $\text{Na}_3\text{V}_2(\text{PO}_4)_2\text{F}_3$ ($\delta = 0$ exactly). This led to a different indexation in the *Amam* space group (Figure 2) and thus to a different structure, preserving the global geometry of the $P4_2/mnm$ framework but showing a different distribution of

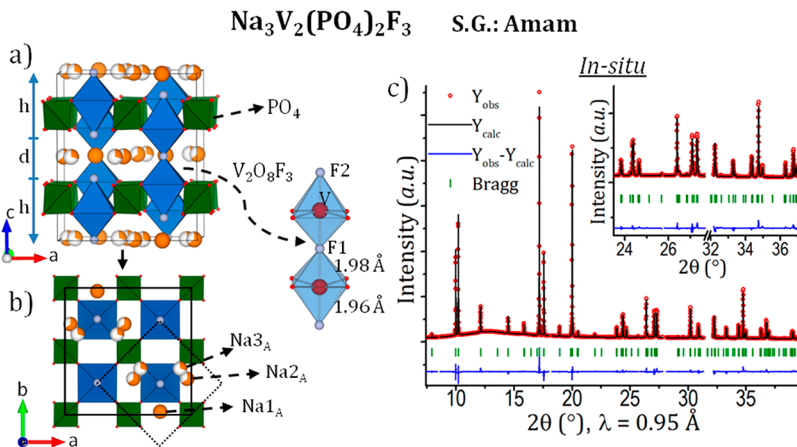


Figure 2. (a) Crystal structure of $\text{Na}_3\text{V}_2(\text{PO}_4)_2\text{F}_3$ in the recently proposed *Amam* space group (ref 26), showing $\text{V}_2\text{O}_8\text{F}_3$ biotahedra, PO_4 tetrahedra, and the three different sites for sodium. The c axis is such that $c = 2h + d$ where h is the height of an octahedron and d the height of sodium tunnels. (b) top view displaying the $a-b$ plane in the case of room temperature unit cell (solid line indicates the associated space group *Amam*, dotted line indicates the unit cell observed at high temperature (400 K), in the space group $I4/mmm$). Orange spheres represent fully occupied Na sites and white/orange spheres partially occupied ones. (c) Rietveld refinement of the structure of $\text{Na}_3\text{V}_2(\text{PO}_4)_2\text{F}_3$ from data collected using our in situ custom cell in transmission geometry.

sodium ions. The arrangement of Na is the key property for this material, and it is at the origin of the orthorhombic distortion. A triangular-like distribution is observed, placed above the terminal fluorine of the biotahedra. Three different sites are present: one fully occupied, Na1_A , and two, Na2_A and Na3_A , partially occupied and pointing toward the tunnel directions as can be seen in Figure 2b (as above the subscript indicates the first letter of the effective space group used).

Both findings—a crystal structure different from the previously accepted one and fine details in the electrochemical data—contrast quite strongly with the available literature on the extraction of sodium from $\text{Na}_3\text{V}_2(\text{PO}_4)_2\text{F}_3$. In fact the reaction mechanism of this material to become $\text{NaV}_2(\text{PO}_4)_2\text{F}_3$ (deintercalation of two sodium ions) has been often described as a solid solution based on ex situ and in situ X-ray diffraction and more recently ab initio calculations and NMR experiments.^{31–36} In other words, every composition x in $\text{Na}_x\text{V}_2(\text{PO}_4)_2\text{F}_3$ ($3 \leq x \leq 1$) ever observed has been simply described in the $P4_2/mnm$ space group, the only one known up to now. We stress that here (and in the following) we will be referring to the phases $\text{Na}_x\text{V}_2(\text{PO}_4)_2\text{F}_3$ ($3 \leq x \leq 1$) and not to $\text{Na}_3\text{V}_2\text{O}_{2\delta}(\text{PO}_4)_2\text{F}_{3-2\delta}$ ($0 \leq \delta \leq 1$). Possible reasons at the origin of these discrepancies are (i) the lack of sufficient angular resolution of diffraction data and (ii) differences in the actual stoichiometry of the pristine samples. In particular the control of the O/F ratio is not straightforward and can result in additional electrochemical features around 3.6 V vs Na^+/Na , related with mixed valence phases of the family $\text{Na}_3\text{V}_2\text{O}_{2\delta}(\text{PO}_4)_2\text{F}_{3-2\delta}$ (the operating voltage decreases as δ increases). Moreover recently published in situ studies showed that for the two compositions $\delta = 1$ and $\delta = 0.8$, which are still supposed to belong to the tetragonal $P4_2/mnm$ space group, the sodium extraction mechanism is far from being a simple solid solution.^{20,37,38} The $\delta = 0.8$ sample ($\text{V}^{3.8+}$) revealed for the first time a biphasic reaction during the lower voltage–composition plateau, while the biggest part of the charging process was modeled as a solid solution.^{20,37} The V^{4+} extreme member ($\text{Na}_3\text{V}_2\text{O}_2(\text{PO}_4)_2\text{F}$, $\delta = 1$) showed instead a sequence of two biphasic reactions upon extraction of the first sodium (hence with observation of an intermediate phase), followed by a long solid solution region and finally another biphasic reaction at the end of charge.³⁸ These observations are actually not surprising since Na-intercalation compounds exhibit a strong tendency to form intermediate phases.^{6,39} For the reasons described above we decided to study the extraction of sodium from $\text{Na}_3\text{V}_2(\text{PO}_4)_2\text{F}_3$ ($\delta = 0$) in a sodium battery (in situ) during operation (operando).

In situ diffraction techniques for the study of Li-ion and more recently Na-ion batteries proved to be invaluable to unambiguously identify reaction dynamics.^{40–43} However, given the complexity of the reactions involved and considering the small orthorhombic distortion of $\text{Na}_3\text{V}_2(\text{PO}_4)_2\text{F}_3$, it appears clearly that high angular resolution (comparable to the one that can be obtained for standard synchrotron measurements in capillaries) is a mandatory requirement for this kind of experiment. We achieved this goal using both the MSPD beamline⁴⁴ at ALBA synchrotron and the electrochemical cell for in situ XRD and XAS measurements in transmission geometry that some of us recently developed.^{45,46} The electrochemical extraction of Na^+ from $\text{Na}_3\text{V}_2(\text{PO}_4)_2\text{F}_3$ was followed in real time, and several phase transitions were identified upon cycling, often involving ordering/disordering phenomena within the sodium ions sublattice. The extremely

good angular resolution and high intensity offered on the MSPD beamline allowed the reaction to be followed with unprecedented details, making full structural Rietveld refinements possible (Figure 2c) and even a first-time crystal structure determination for the end member $\text{NaV}_2(\text{PO}_4)_2\text{F}_3$ directly from in situ (operando) diffraction data.

METHODS

The synthesis of $\text{Na}_3\text{V}_2(\text{PO}_4)_2\text{F}_3$ followed a two-step procedure adapted from the one patented by Barker et al.⁴⁷ and analogous to the one that we recently reported (all details can be found in ref 26). The combination of different characterization techniques (XRD, neutron diffraction, ICP-OES, SQUID, SEM analysis, and electrochemical tests in sodium batteries) have also shown that the pristine material used in this study is identical to the previously published one.²⁶

Electrodes were prepared mixing $\text{Na}_3\text{V}_2(\text{PO}_4)_2\text{F}_3$ with Carbon Super P (C_{sp}) as a conductive additive and polyvinylidene fluoride (PVDF) as a binder (84:10:6 wt %) and grinding them in a mortar until a homogeneous paste was obtained. Small pellets of ~5 mm diameter and ~300 μm thickness were used in our in situ cell.⁴⁵ The use of a binder is fundamental because it allows overcoming the problem of spatially inhomogeneous electrodes observed while cycling in the in situ cell.⁴⁶ The active part of the cell is composed of layers of positive electrode, glass fiber separators (Whatman) wet with 1 M NaPF_6 in EC:PC (1:1) electrolyte, and sodium metal as a counter electrode. The stack is inserted between two Beryllium windows, acting as X-ray-transparent current collectors. The internal pressure within the cell is applied through a spring to ensure optimal electrical contact.

Two batteries were prepared in two separate in situ cells. The first voltage–composition plateau was measured using a GITT (Galvanostatic Intermittent Titration Technique) protocol, for which steps of 5 min of charge and 5 min of relaxation are alternated. During charging steps, the current rate was set to be C/5 (extraction of 1 Na^+ ion in 5 h in this case). At constant current rate, change in composition (Δx) is directly proportional to charging time (Δt): $\Delta x = \Delta t \times I \times (M_w/Fm)$, where F is Faraday's constant, m the active mass of electrode material, M_w its molecular weight, and I the current. Upon cycling, 5 min diffraction scans were continuously recorded during the 5' charge–5' relaxation sequence. For the observation of the second voltage–composition plateau, the second cell was cycled off-line through the first voltage–composition plateau and kept at the composition $\text{Na}_2\text{V}_2(\text{PO}_4)_2\text{F}_3$ until we could mount it on the instrument. Since in the first experiment we did not observe any significant evolution between subsequent scans recorded upon charge and relaxation, a continuous electrochemical cycling at C/5 rate was used (with 10 min relaxation times every 0.25 Na^+ exchange), while recording again diffraction scans continuously every 5 min.

Operando synchrotron radiation diffraction measurements were performed at the MSPD beamline⁴⁴ of the ALBA synchrotron in Cerdanya del Valles, Spain. Transmission geometry was used, with the beam going through all the layers of the cell. Throughout all the experiment, the operating wavelength was $\lambda = 0.9535(1)$ \AA refined using a NIST standard silicon sample (NIST SI640D). Such a relatively long wavelength was specifically chosen in order to minimize peak overlap and in particular to better resolve reflections characteristic of the orthorhombic distortion. Powder diffraction patterns were collected using the one-dimensional silicon based position sensitive detector MYTHEN in the 2–50° angular 2 θ range (d -range: 1.12–40 \AA). Since MYTHEN detector spans a ~40° angular 2 θ range, this setup allows fast data acquisition with extremely high statistics and good angular resolution. The full width at half-maximum (fwhm) for representative peaks of the pristine phase is 0.022° at $2\theta = 17.15^\circ$ (increasing to 0.04° toward the highest angles), and the signal-to-noise ratio for the most intense peak amounts to ~36. The quality of the data collected in these conditions allows Rietveld structural refinements of all the identified phases with goodness comparable to refinements performed using the highest angular resolution mode reported in ref 26. Table S1 (given as Supporting Information)

compares refinements outputs of the pristine phase from data collected in capillaries with actual results obtained using the in situ cell setup. It can be noted that the use of the in situ cell only slightly increases the error bars, allowing refinement of all atomic parameters, including isotropic thermal factors B_{iso} (constraint to be equal for the same type of atoms) and site occupancy factors (SOFs) for sodium. However, when performing Rietveld refinements on data collected using the in situ cell a few precautions have to be taken:

- The beam is going through all layers in the battery, generating Bragg peaks from sodium (often textured) and beryllium (two windows displaced one with respect to the other). Detailed knowledge of the pristine phase allows eliminating the (narrow) 2θ regions where these peaks occur. Supporting Information Figure S1 shows the full measured 2θ range, indicating the position of the extra-Bragg peaks.
- Each layer suffers differently from X-ray absorption. Beryllium is a light element, and its absorption (0.24 cm^{-1}) can be neglected at this energy. Sodium metal is heavier but the absorption (24.9 cm^{-1}) can still be neglected as sodium is crossed before the sample. Absorption from the sample itself is instead important, and it is taken into account using the correction factor for flat-plate samples in transmission geometry implemented in the Fullprof suite (approximately $mt = 1$, where $m = 36.7 \text{ cm}^{-1}$ is the absorption and $t = 300 \mu\text{m}$ is the sample's thickness).
- Because the sample is enclosed in the in situ cell, hence not visible, it is impossible to precisely position the sample in the center of the goniometer by standard optical alignment means. To correctly refine the data, both a zero-shift and a systematic shift ($\sin\theta$ dependence) correction are hence needed to compensate possible misalignment of the sample. As a first step we thus used the pristine $\text{Na}_3\text{V}_2(\text{PO}_4)_2\text{F}_3$, whose unit cell parameters are well-known, to determine zero-shift and systematic shift. As a second step we fixed these two parameters throughout all the subsequent refinements. Data treatment and Rietveld refinement⁴⁸ were performed using the Fullprof Suite.⁴⁹

A sample of nominal composition $\text{Na}_2\text{V}_2(\text{PO}_4)_2\text{F}_3$ was also prepared ex situ by chemically oxidizing $\text{Na}_3\text{V}_2(\text{PO}_4)_2\text{F}_3$ with nitronium tetrafluoroborate (NO_2BF_4) in acetonitrile media. The resulting powder was washed, sealed in a 0.5 mm diameter capillary, and then measured under the same experimental conditions.

RESULTS AND DISCUSSION

As described above (Figure 1), sodium ions are extracted from the framework of $\text{Na}_3\text{V}_2(\text{PO}_4)_2\text{F}_3$ through two different voltage regions, a lower one around 3.7 V vs Na^+/Na and a higher one around 4.2 V vs Na^+/Na . Given the incredibly rich phase diagram found and analyzed in this study (Figure 3) and for sake of clarity, the two voltage domains are discussed separately. Additionally, each definite $\text{Na}_x\text{V}_2(\text{PO}_4)_2\text{F}_3$ composition will be labeled as Na_xVPF in the following.

A. $\text{Na}_3\text{V}_2(\text{PO}_4)_2\text{F}_3$ – $\text{Na}_2\text{V}_2(\text{PO}_4)_2\text{F}_3$ System (~3.7 V vs Na^+/Na). Figure 4 shows the XRD patterns recorded during GITT relaxation intervals, upon extraction of sodium from Na_3VPF until the composition Na_2VPF is reached at the end of the first voltage–composition domain. Note the very high quality of the diffracted data, in terms of both angular and intensity resolution, essential for identifying tricky phenomena occurring in this system. It immediately appears that no continuous shifts in diffracted peak positions occur during this first electrochemical region: those of the pristine phase Na_3VPF lose intensity right away, while new ones start growing. Specific compositions and their corresponding XRD patterns are highlighted with colored circles indicating the amount of Na/f.u. (determined from electrochemistry in this case, as described

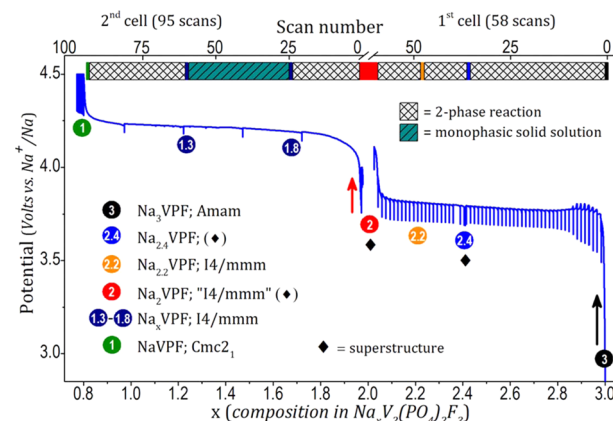


Figure 3. Potential–composition electrochemical curves obtained upon Na^+ extraction from Na_3VPF . The first cell was cycled (GITT) between the compositions Na_3VPF and Na_2VPF while recording 58 5 min diffraction scans; the second one (galvanostatic cycling) between the compositions Na_2VPF and Na_1VPF while recording 95 5 min scans. Significant single-phase compositions are highlighted by colored circles. For the first cell they are obtained by the electrochemistry. Cycling of the second cell resulted in $\Delta x > 1$ because of electrolyte oxidation, hence in this case reported compositions are those obtained from Rietveld refinement. Top line describes the nature of the observed deintercalation mechanism.

in the Methods section). These are $\text{Na}_{2.4}\text{V}_2(\text{PO}_4)_2\text{F}_3$ ($\text{Na}_{2.4}\text{VPF}$), $\text{Na}_{2.2}\text{V}_2(\text{PO}_4)_2\text{F}_3$ ($\text{Na}_{2.2}\text{VPF}$), and $\text{Na}_2\text{V}_2(\text{PO}_4)_2\text{F}_3$ (Na_2VPF), corresponding to new single phases found in this subsystem, and they are discussed in the following. Besides the obvious correlated appearances/disappearances of these phases (Figure 4), a peculiar attention was paid to reflections of weaker intensities (Figure 4b) which usually act as indicators of the presence/absence of sodium/vacancy ordering within the framework. We indeed previously observed such a phenomenon for Na_3VPF by determining its crystal structure at 298 K (orthorhombic *Amam*) and 400 K (tetragonal *I4/mmm*).²⁶ Sodium ions disorder upon heating and adopt a “circular” arrangement above fluorine anions, inducing the material to adopt a more symmetrical space group and thus to lose several weak reflections.

The detailed evolution of specific Bragg peaks in the two-phase region Na_3VPF – $\text{Na}_{2.4}\text{VPF}$ is depicted in Figure 5. From the very beginning of Na^+ extraction, large “shoulders” appear on the right side of the reflections of Na_3VPF , progressively revealing an internal structure, where at least three distinct diffraction peaks can be noticed (scan no. 30). These reflections remain broad, indicating that the reaction crosses different intermediate states (probably metastable) where sodium partially orders on the short-medium range only, until reaching the composition $\text{Na}_{2.4}\text{VPF}$. A close examination of the data reveals as well the appearance of additional weak-intensity diffraction peaks for $\text{Na}_{2.4}\text{VPF}$, in particular at a 2θ value of 3° ($d_{hkl} \sim 18 \text{ \AA}$, shown on Figure 4b), which suggests a doubling of the unit cell (superstructure) in the a or b directions (or both) due to Na^+ /vacancy and/or $\text{V}^{3+}/\text{V}^{4+}$ possible ordering. Considering that the values of a and b were 9.026 and 9.042 \AA , respectively, in the Na_3VPF pristine phase (Table 1), the d -spacing of 18 \AA ($2 \times 9 \text{ \AA}$) in $\text{Na}_{2.4}\text{VPF}$ is consistent with the oxidation of vanadium from V^{3+} to “ $\text{V}^{3.3+}$ ” (shorter in-plane bonds). However, no complete indexation was found for this phase because a simple doubling of any of the unit cell parameters could not explain all observed reflections. We

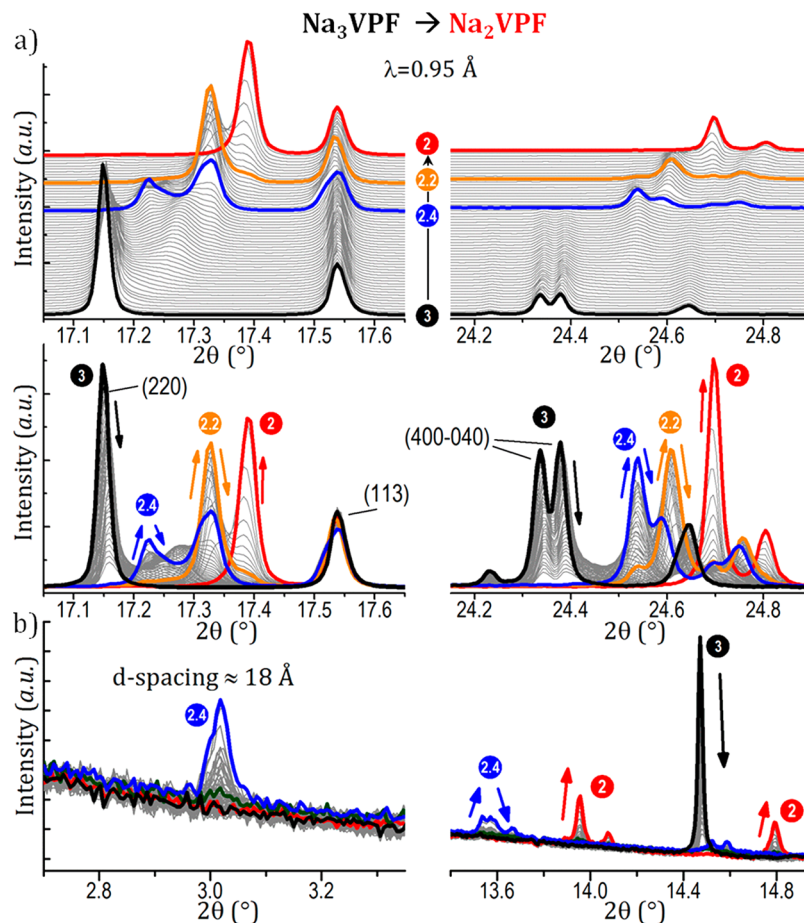


Figure 4. Different angular domains observed during the extraction of 1 Na^+ from Na_3VPF (black curve). Several single-phase compositions are formed through biphasic domains, namely, $\text{Na}_{2.4}\text{VPF}$ (blue), $\text{Na}_{2.2}\text{VPF}$ (orange), and Na_2VPF (red). (a) $17^\circ - 17.7^\circ$ (left) and $24.1^\circ - 24.9^\circ$ (right) angular domains. Peaks are indexed for the Na_3VPF phase. (b) $2.7^\circ - 3.3^\circ$ and $13.5^\circ - 14.9^\circ$ angular domains (weak peaks related to sodium ordering).

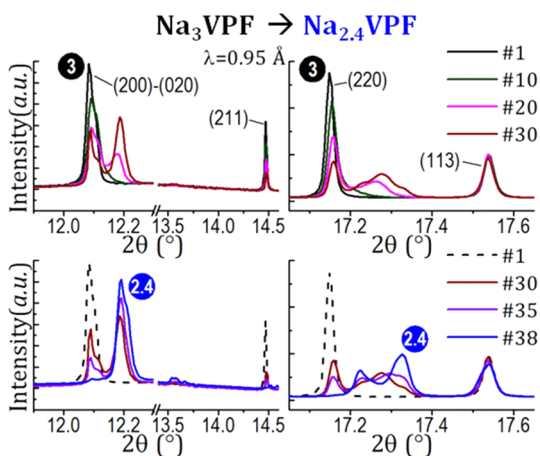


Figure 5. Detailed view of the initial stages of sodium deintercalation. Selected patterns from no. 1 (Na_3VPF) to no. 38 ($\text{Na}_{2.4}\text{VPF}$) are presented in the $11.9^\circ - 14.55^\circ$ and $17^\circ - 17.7^\circ$ angular domains. A complex behavior can be noticed in the structured shape of the peaks $(200)-(020)$ and (220) . Other peaks as (211) disappear (effect of sodium disordering), while some are almost unaffected (113) .

believe this composition is in fact not fully “stabilized” and that it still contains domains which have not reached complete ordering.

Once the $\text{Na}_{2.4}\text{VPF}$ composition is reached, the deintercalation reaction proceeds again as a biphasic one (Figure 4 and Figure 6) toward a newly isolated single phase, $\text{Na}_{2.2}\text{VPF}$. This phase is interesting as it shows no extra weak reflections (loss of the superstructure observed for $\text{Na}_{2.4}\text{VPF}$) and displays a rather “simple” XRD pattern: the characteristic peaks of the orthorhombic Na_3VPF due to Na^+ ordering are absent in $\text{Na}_{2.2}\text{VPF}$, fully indexed using the $I4/mmm$ space group. Overall, from Na_3VPF to $\text{Na}_{2.2}\text{VPF}$ (passing through $\text{Na}_{2.4}\text{VPF}$), the unit cell volume decreases from $V/Z = 219.39(1) \text{ \AA}^3$ to $V/Z = 215.66(1) \text{ \AA}^3$ which appears somewhat small ($\Delta V/V = -1.7\%$) since a strong anisotropy in lattice parameters variations occurs: $\Delta a/a = -0.92\%$; $\Delta b/b = -1.10\%$; $\Delta c/c = +0.38\%$ (Table 1). The crystal structure of $\text{Na}_{2.2}\text{VPF}$ was refined by the Rietveld method (Figure 7). Sodium ions adopt a disordered arrangement, and Fourier difference maps (reported in Supporting Information Figure S2) reveal that both Na1_1 and Na2_1 sodium positions are occupied, leading to a refined composition of $x = 2.3(2)$, in good agreement with the electrochemical data ($x = 2.2$). These refinements show, interestingly, that the above-mentioned variation of the cell parameter c (between Na_3VPF and $\text{Na}_{2.2}\text{VPF}$) is opposite to the shortening of the V–F bond lengths along the F–V–F–V–F chain in the bioctahedra (Table 2): V–F1 decreases from $1.981(2) \text{ \AA}$ to $1.953(5) \text{ \AA}$ and V–F2 decreases from $1.968(6) \text{ \AA}$ to $1.91(1) \text{ \AA}$, as expected for

Table 1. Compositions Obtained upon Na^+ Extraction from Na_3VPF^a

composition	S. G.	a (\AA)	b (\AA)	c (\AA)	vol. (\AA^3)	V/Z (\AA^3)
$\text{Na}_3\text{V}_2(\text{PO}_4)_2\text{F}_3$ (ref 26)	<i>Amam</i>	9.02847(3)	9.04444(3)	10.74666(6)	877.544(6)	219.386(6)
$\text{Na}_3\text{V}_2(\text{PO}_4)_2\text{F}_3$ (<i>in situ</i>)	<i>Amam</i>	9.0262(1)	9.0418(2)	10.7434(3)	876.80(1)	219.20(1)
$\text{Na}_{2.4}\text{V}_2(\text{PO}_4)_2\text{F}_3$				structure not determined		
$\text{Na}_{2.2}\text{V}_2(\text{PO}_4)_2\text{F}_3$	<i>I4/mmm</i>	6.3244(1)	6.3244(1)	10.7837(3)	431.33(1)	215.66(1)
$\text{Na}_{2.2}\text{V}_2(\text{PO}_4)_2\text{F}_3$	<i>I4/mmm</i> (average unit cell)	6.3021(1)	6.3021(1)	10.7933(2)	428.67(1)	214.34(1)
$\text{Na}_{2.2}\text{V}_2(\text{PO}_4)_2\text{F}_3$	<i>Pmmm</i> (considering a superstructure) ^b	25.221(1)	12.599(1)	21.586(1)	6859.42(3)	214.36(3)
$\text{Na}_{1.8}\text{V}_2(\text{PO}_4)_2\text{F}_3$ (solid sol.)	<i>I4/mmm</i>	6.2800(1)	6.2800(1)	10.8493(3)	427.88(1)	213.94(1)
$\text{Na}_{1.3}\text{V}_2(\text{PO}_4)_2\text{F}_3$ (solid sol.)		6.2481(1)	6.2481(1)	10.9222(2)	426.39(1)	213.19(1)
$\text{NaV}_2(\text{PO}_4)_2\text{F}_3$	<i>Cmc2_1</i>	8.7822(3)	8.7962(3)	11.0015(2)	849.86(1)	212.47(1)

^aSpace groups, cell parameters, and volumes are reported. ^bThe actual space group of composition Na_2VPF in its superstructural arrangement is not known, so the low-symmetry space group *Pmmm* is used to index all observed reflections.

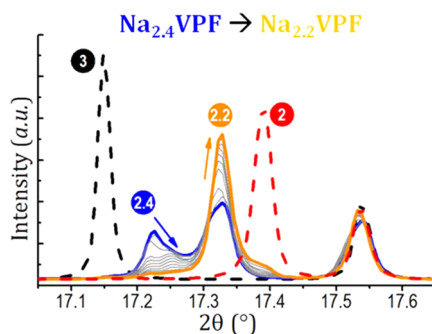


Figure 6. Detailed view of the biphasic reaction between scans no. 38 ($\text{Na}_{2.4}\text{VPF}$) and no. 47 ($\text{Na}_{2.2}\text{VPF}$). At this composition only two peaks at 17.33° and 17.54° remain, characteristic of the *I4/mmm* space group.

the oxidation of vanadium. Considering the model used in ref 27 ($c \sim 2h + d$ with h = height of an octahedron and d = height of sodium's tunnels, Figure 2), we notice a significant increase in the value of d . In fact, d varies from $2.86(1)$ \AA for the pristine Na_3VPF phase to $3.06(1)$ \AA for $\text{Na}_{2.2}\text{VPF}$. The increase in the value of c is mainly due to the increased electrostatic repulsion between subsequent bioctahedra, caused by a smaller global screening effect of sodium.

The final reaction observed in the 3.7 V vs Na^+/Na region is again a biphasic one. The XRD peaks of $\text{Na}_{2.2}\text{VPF}$ disappear while new peaks belonging to the Na_2VPF end-member appear (Figure 4). A first look at the 24° – 25° 2θ region shows that the splitted (400) and (040) peaks of Na_3VPF are again merged into one single peak in Na_2VPF , suggesting a tetragonal space group. A more detailed look reveals however that this phase generates many extra weak reflections that can be observed in the 13.4° – 15° (Figure 4b) and 6° – 21° (Figure 8) 2θ domains. Neglecting the weakest peaks, the reflections can be indexed with an “average” cell using the high-symmetry *I4/mmm* space group ($a = 6.3021(1)$ \AA , $c = 10.7933(2)$ \AA). At present, a complete indexation of the XRD pattern for Na_2VPF could be found only for a huge superstructure cell of $a' = 25.221(1)$ \AA , $b' = 12.599(1)$ \AA , and $c' = 21.586(1)$ \AA (shown in Supporting Information Figure S3), i.e., with $a' = 4a$, $b' = 2b$, $c' = 2c$ ($V_{\text{super}} = 16V_{\text{sub}}$) with respect to the cell parameters of $\text{Na}_{2.2}\text{VPF}$. Such a large unit cell can be explained assuming that not only sodium ions adopt some sort of ordering, but vanadium cations do the same (V^{3+} and V^{4+}) as the average oxidation state of V within Na_2VPF is $\text{V}^{3.5+}$. To verify the reproducibility of our *in situ* data we prepared Na_2VPF *ex situ* (Figure 8), by chemical oxidation of Na_3VPF , yielding a powder

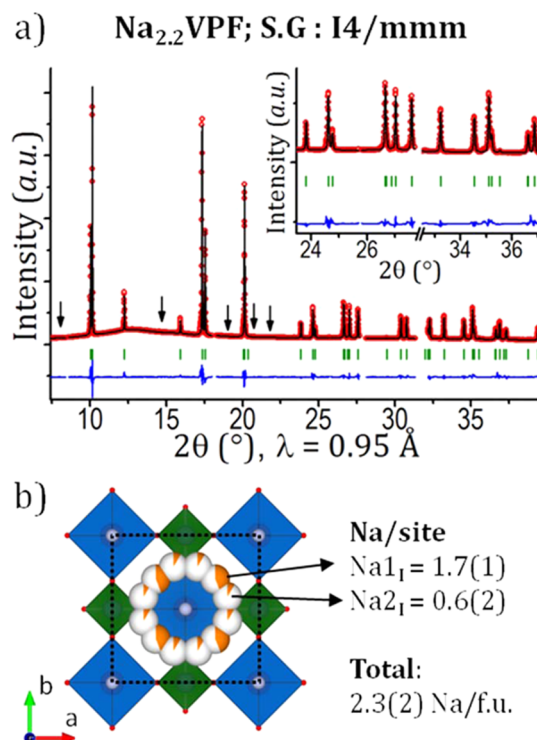


Figure 7. (a) Rietveld refinement of the intermediate phase $\text{Na}_{2.2}\text{VPF}$. Missing reflections related to sodium ordering in Na_3VPF (S.G.: *Amam*) are indicated by arrows. (b) Crystal structure of $\text{Na}_{2.2}\text{VPF}$, refined in the *I4/mmm* space group. Two sites $\text{Na}_{1,1}$ and $\text{Na}_{2,1}$ are present for sodium. Their occupancy is refined, and the related sodium amount is reported.

with very similar unit-cell parameters and superstructure reflections. At present, and in the following of the paper, we treated Na_2VPF in the “average” tetragonal unit cell, which gives meaningful results (parameters reported in Table 1 and Table 2). Importantly, Fourier difference maps (Supporting Information Figure S4) do not show any intensity on the $\text{Na}_{2,1}$ site, leaving only the square-like distribution generated by the $\text{Na}_{1,1}$ site (its occupancy can be refined to give $2.05(6)$ Na/f.u., Supporting Information Figure S4). This is however only an “average” distribution, and several first principle calculations^{20,27,29,31} predicted that instead of four half-occupied positions (generated by the same crystallographic site) it is favorable for sodium to arrange in two fully occupied positions (trans arrangement), alternated so as to minimize the electrostatic repulsion. The fact that we observe a superstructure is in good agreement with these studies, and the

Table 2. Bond Lengths and Sodium Content/Formula Unit Obtained from Rietveld Refinement of Selected Deintercalated Phases Observed *in Situ* during Na^+ Extraction from Na_3VPF

composition	refined Na/f.u.	V–F1	V–F2	V–O1	V–O2
$\text{Na}_3\text{V}_2(\text{PO}_4)_2\text{F}_3$ (ref 26)	2.9(2)	1.981(2)	1.968(6)	2.006(9)	1.965(9)
$\text{Na}_3\text{V}_2(\text{PO}_4)_2\text{F}_3$ (<i>in situ</i>)	3.0(2)	1.985(3)	1.938(9)	2.00(1)	2.00(1)
$\text{Na}_{2.2}\text{V}_2(\text{PO}_4)_2\text{F}_3$	2.3(2)	1.953(5)	1.91(1)	1.954(6)	1.954(6)
$\text{Na}_2\text{V}_2(\text{PO}_4)_2\text{F}_3$ (<i>I4/mmm</i>)	2.05(7)	1.947(4)	1.88(1)	1.946(6)	1.946(6)
$\text{Na}_{1.8}\text{V}_2(\text{PO}_4)_2\text{F}_3$	1.85(7)	1.932(5)	1.92(1)	1.926(9)	1.926(9)
$\text{Na}_{1.3}\text{V}_2(\text{PO}_4)_2\text{F}_3$	1.31(6)	1.938(4)	1.87(1)	1.942(6)	1.942(6)
$\text{NaV}_2(\text{PO}_4)_2\text{F}_3$	0.88(9)	V1: 2.00(9)	V1–F3: 1.67(4)	V1–O1: 1.86(6)	V1–O2: 1.89(6)
		V2: 1.88(9)	V2–F2: 2.02(3)	V2–O3: 1.92(6)	V2–O4: 2.09(5)

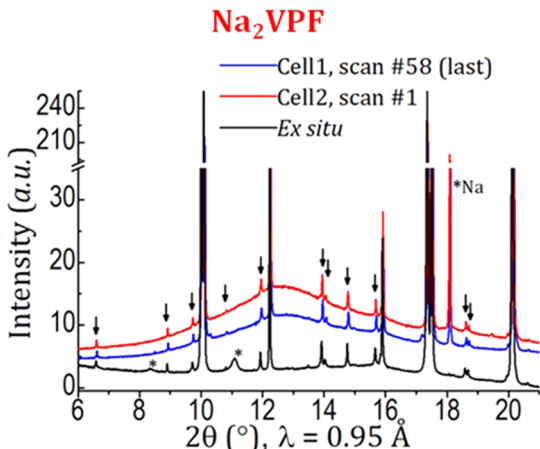


Figure 8. Comparison of composition Na_2VPF obtained by ex situ chemical oxidation (black), *in situ* in the first electrochemical cell (blue, after diffraction measurements across the low-voltage-composition plateau), and *in situ* in the second electrochemical cell (red, before diffraction measurements across the high-voltage-composition plateau). The same Bragg reflections are observed. An * marks peaks not belonging to phase Na_2VPF (originating from sodium metal in the *in situ* experiments; from an impurity left as residue of the chemical preparation in the ex situ sample).

actual structure determination of Na_2VPF will possibly confirm them. We are confident that our observation of a large unit cell combining different types of orderings will stimulate further research especially in terms of DFT and ab initio calculations, in order to propose an adequate crystal structure for Na_2VPF .

A close look at the correspondence between the electrochemical and diffraction data reveals a somewhat puzzling behavior. As can be seen in the inverse derivative curve of Figure 1, the Na^+ extraction from Na_3VPF to Na_2VPF seems composed of two features at 3.68 and 3.70 V vs Na^+/Na (i.e., separated by only 20 mV), suggesting a sequence of two biphasic reactions with an intermediate phase around the composition $\text{Na}_{2.4}\text{V}_2(\text{PO}_4)_2\text{F}_3$. However, our structural data recorded *in situ* point toward three biphasic reactions Na_3VPF – $\text{Na}_{2.4}\text{VPF}$, $\text{Na}_{2.4}\text{VPF}$ – $\text{Na}_{2.2}\text{VPF}$, and $\text{Na}_{2.2}\text{VPF}$ – Na_2VPF . A similar case of electrochemistry/diffraction “disagreement” (or “difference in sensitivity”) was recently reported for the Na^+ extraction from NaFePO_4 , toward an intermediate phase $\text{Na}_{2/3}\text{FePO}_4$. This intermediate phase is observed by diffraction both upon charge and subsequent discharge, while it is hardly expected from the shape of the voltage–composition electrochemical curve on discharge. This asymmetry phenomenon was tentatively attributed by the authors to different lattice mismatches.^{7,8,43} In our case the two compositions $\text{Na}_{2.4}\text{VPF}$ and $\text{Na}_{2.2}\text{VPF}$ are so close to each

other in energy that they cannot be differentiated from their electrochemical (voltage) signature, even at extremely relaxed GITT conditions (see Supporting Information Figure S5). The $\text{Na}_{2.4}\text{VPF}$ composition is able to stabilize a long-range order ($2/3 \text{V}^{3+}$, $1/3 \text{V}^{4+}$, for example) suppressed in $\text{Na}_{2.2}\text{VPF}$, even if local orders might be maintained.

B. $\text{Na}_2\text{V}_2(\text{PO}_4)_2\text{F}_3$ – $\text{Na}_{1.8}\text{V}_2(\text{PO}_4)_2\text{F}_3$ System (~4.2 V vs Na^+/Na). To study the higher voltage domain, i.e., the extraction of sodium from Na_2VPF to NaVPF , a second electrochemical cell was cycled off-line until $\text{Na} = 2$ composition was reached and then placed in the beam. The evolution of Bragg’s reflections when Na^+ is extracted from Na_2VPF is shown in Figure 9. The diffraction peaks of the pristine phase Na_2VPF lose intensity right away (red curve), while new ones start growing. Specific compositions and their corresponding XRD patterns are highlighted again with colored circles indicating the amount of Na/f.u. (determined from XRD in this case, since from galvanostatic cycling we notice that the theoretical capacity $\Delta x = 1$ is exceeded because of partial electrolyte oxidation). We discuss in the following the new single phases found in this subsystem, which are $\text{Na}_2\text{V}_2(\text{PO}_4)_2\text{F}_3$ (Na_2VPF), $\text{Na}_x\text{V}_2(\text{PO}_4)_2\text{F}_3$ (Na_xVPF , $1.8 \leq x \leq 1.3$), and $\text{Na}_1\text{V}_2(\text{PO}_4)_2\text{F}_3$ (NaVPF).

In the early stage of Na^+ extraction from Na_2VPF , the weakest diffraction peaks disappear, most likely because of sodium and vanadium cations disordering in the structure (Figure 9b). The dV/dx shoulder at 4.16 V vs Na^+/Na (Figure 1) corresponds to a biphasic first order reaction that could be easily mistaken for a second order one due to the extreme vicinity of the disappearing peaks of Na_2VPF with those of the growing phase $\text{Na}_{1.8}\text{VPF}$. However, the latter misses some of the reflections of the former, leaving no doubt about the reaction mechanism. Interestingly, in the Na_2VPF – $\text{Na}_{1.8}\text{VPF}$ miscibility gap, the cell parameters of both phases continue to vary (results from Rietveld refinement in Figure 10), although this would be in principle thermodynamically forbidden (in equilibrium conditions a biphasic reaction implies that the two phases—the sodium-rich and the sodium-poor—change in relative weight but not in the amount of sodium in every phase, thus keeping constant cell parameters). This is directly observable in Figure 9 where the diffracted reflections from Na_2VPF (in red) lose intensity but also shift concurrently (although in absolute values the variation of cell parameters during that two-phase region is only of 0.01 \AA to 0.02 \AA). Such a behavior has been recently reported for several materials as an effect induced by particle size, strains, and high-rate (non-equilibrium) cycling conditions.^{42,50–53} In our case the battery charged rather slowly (C/5 per Na^+) and the volume change from Na_2VPF to $\text{Na}_{1.8}\text{VPF}$ is only $\Delta V/V = -0.2\%$. At present we do not have any obvious hypothesis to explain this puzzling

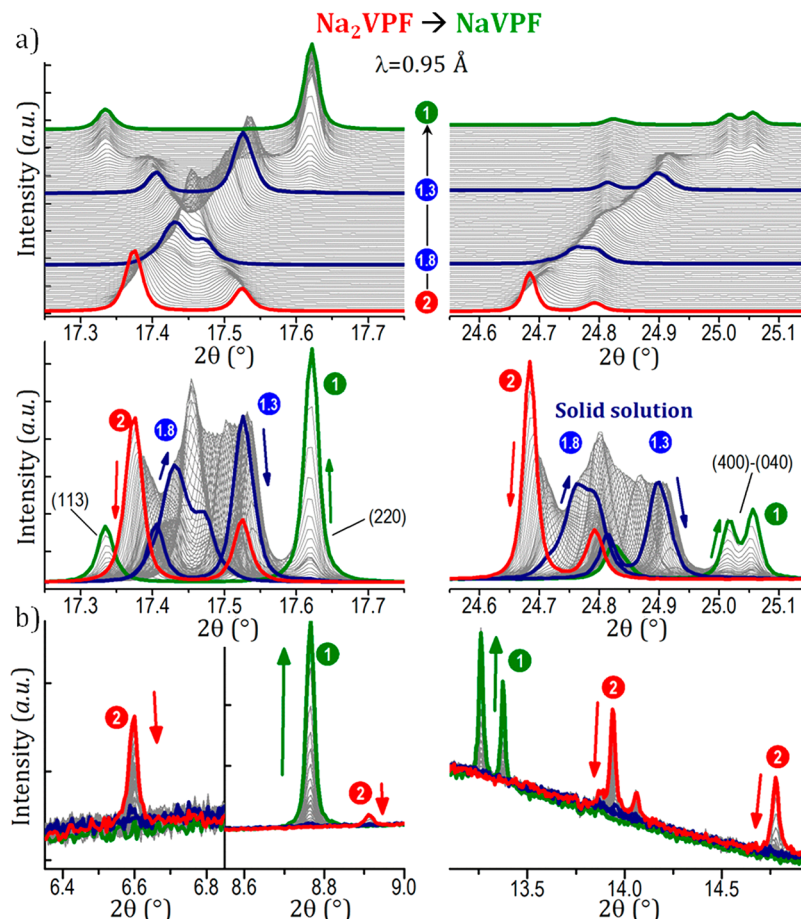


Figure 9. Different angular domains observed during the extraction of 1 Na⁺ from Na₂VPF (red curve). Na₂VPF disappears through a biphasic reaction, and then a solid solution is present between Na_{1.8}VPF and Na_{1.3}VPF (both in dark blue); finally Na₁VPF (green curve) crystallizes through a biphasic reaction. (a) 17.25°–17.75° (left) and 24.55°–25.15° (right) angular domains. Peaks are indexed for the Na₁VPF phase. (b) 6.4°–6.8°, 8.6°–9.0°, and 12.9°–14.9° angular domains (weak peaks related to sodium ordering).

lattice parameters' variation within a biphasic electrochemical process.

The single phase Na_{1.8}VPF is sodium-disordered and undergoes a solid solution reaction upon further Na⁺ extraction within the Na_xVPF (1.8 ≤ x ≤ 1.3) compositional range. All reflections can be indexed using the I4/mmm space group. A sequential Rietveld refinement procedure was undertaken (Figures 10 and 11). The *a* and *b* lattice parameters continuously decrease from 6.2800(1) Å to 6.2481(1) Å, while *c* increases (more significantly) from 10.8493(3) Å to 10.9222(2) Å, leading to characteristic Bragg peak crossings (see 17.4°–17.6° 2θ region in Figure 9). All fractional atomic coordinates and the site occupancy factor (SOF) for sodium in the Na₁ site were refined (Figure 11). SOF is a particularly useful parameter because it offers a direct observation of the amount of sodium present in the unit cell. The total number of Na⁺ within the Na₁ equivalent crystallographic positions decreases from 1.85(7) for Na_{1.8}VPF to 1.31(6) Na/f.u. for Na_{1.3}VPF. The V–F bond lengths vary anisotropically (1.932(5) Å to 1.938(4) Å for V–F1, 1.92(1) Å to 1.87(1) Å for V–F2) as often encountered during vanadium oxidation,^{12,50} while V–O increases slightly from 1.926(9) Å to 1.942(9) Å (Table 2). It is interesting to observe the distortion of vanadium's octahedral environment (Figure 11), which increases by a factor 30 during this solid solution process, mainly due to the continuous shortening of the V–F2 bond.

The end of charge occurs through a biphasic reaction between Na_{1.3}VPF and NaVPF at 4.19 V vs Na⁺/Na (Figure 1). Extra reflections at low 2θ angles indicate the formation of a new sodium-ordered phase, NaVPF (Figure 9b). The reaction between Na_{1.3}VPF and NaVPF is peculiar because it shows a delay. NaVPF starts forming promptly, but its crystallization is not evolving linearly. A possible explanation is that this phase nucleates in the form of stable small domains spread in the sample, making it hardly detectable by diffraction. As the process goes on, the domains either grow and/or coalesce until a long-range NaVPF crystalline structure is observed. This process can be understood in view of the proposed NaVPF crystal structure as will be discussed in more detail at the end of the next paragraph. The diffraction pattern of the obtained NaVPF phase does not correspond to any of those previously encountered. Cell parameters reveal a certain similarity with the pristine phase because of a subtle orthorhombic distortion: *a* = 8.7822(3) Å, *b* = 8.7962(3) Å, *c* = 11.0015(2) Å, that can be noticed in the right part of Figure 9 (in green, peaks (400) and (040)). This indicates an extremely small volume change $\Delta V/V = 3\%$ along the overall charge of the material (Table 1). Systematic extinctions reveal a C-centered space group for the crystal structure of NaVPF and the space groups showing the best results from profile-matching are Cmcm, Cmc₂₁, and C2cm in setting 1. A structural determination in space groups Cmcm and C2cm was attempted without success, while Cmc₂₁ (a

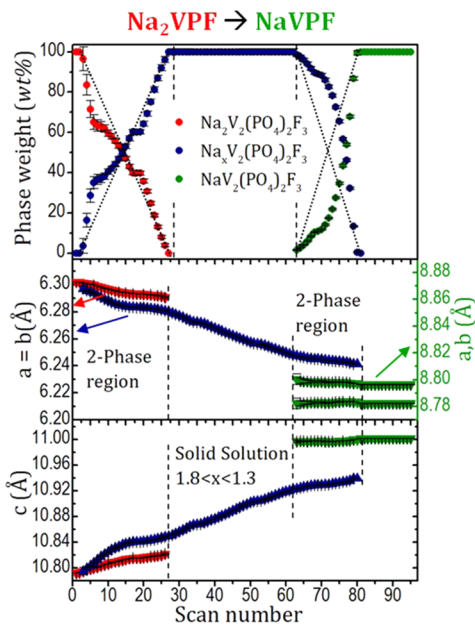


Figure 10. Parameters obtained from Rietveld refinement during the high-voltage–composition plateau (electrode reacting from composition Na_2VPF to NaVPF). Unit cell parameters of the different phases and relative percentage in weight are presented. All the phases were described in the space group $I4/mmm$, except NaVPF in $Cmc2_1$.

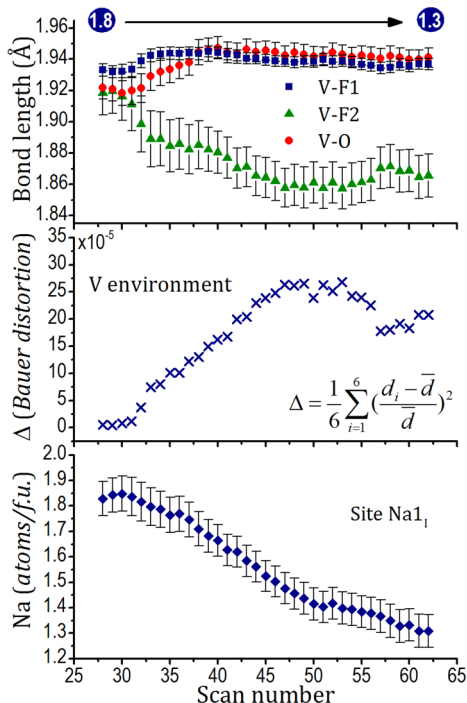


Figure 11. Parameters obtained from Rietveld refinement (S.G. $I4/mmm$) during the solid solution reaction occurring in Na_xVPF ($1.8 \leq x \leq 1.3$). Top: vanadium's bond lengths obtained from refinement of fractional atomic coordinates. Middle: Bauer distortion calculated for VO_4F_2 octahedra. Bottom: amount of sodium/formula unit obtained from the refined site occupancy factor in site $\text{Na}1_1$.

subgroup of $Cmcm$) allowed us to obtain a structure related to the pristine one, showing V bioctahedra and PO_4 tetrahedra. This description requires a shift of the unit cell origin of $(1/4, 0, 0)$ with respect to the pristine one, placing V in two different

4a Wyckoff positions and generating two different V environments (Figure 12). Rietveld refinement (reported with relative

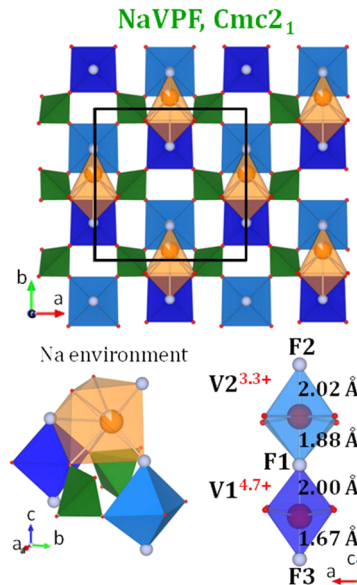


Figure 12. Structure of NaVPF (full composition $\text{NaV}_2(\text{PO}_4)_2\text{F}_3$) in the $Cmc2_1$ space group. Two different environments for vanadium cations are observed (dark and light blue), suggesting a V^{3+} – V^{5+} pair (oxidation state from BVS calculations is displayed). Environment of sodium in a capped prism is also reported.

Fourier maps in Supporting Information Figure S6) indeed showed that the two vanadium belonging to the same bioctahedron have different environments: bond-valence sum calculations clearly differentiate them into a V^{3+} – V^{5+} -type pair (+4.7(3) for V1 and +3.3(2) for V2) rather than into a V^{4+} – V^{4+} one. More than two oxidation states of vanadium have already been shown to coexist in the same material, and vanadium's disproportionation is an occurring reaction ($2\text{V}^{4+} \rightarrow \text{V}^{3+} + \text{V}^{5+}$). As an example, it was found for $\text{Li}_{1+x}\text{V}_3\text{O}_8$ that upon reduction (Li insertion) the signature of V^{3+} can coexist with the V^{4+} and V^{5+} ones.⁵⁴ In the same way, the coexistence of V^{3+} and V^{5+} has also been observed using XANES spectroscopy for $\text{NaV}_2^{4.8}\text{O}_{1.6}(\text{PO}_4)_2\text{F}_{1.4}$, obtained by sodium deintercalation from the pristine compound $\text{Na}_3\text{V}_2^{3.8}\text{O}_{1.6}(\text{PO}_4)_2\text{F}_{1.4}$:⁵⁵ the signature of V^{3+} is reported to be present with those of V^{4+} and V^{5+} . The authors proposed that the small amount of V^{3+} present in the pristine material would not be involved in the redox processes, but considering our results obtained for $\text{NaV}_2^{4+}(\text{PO}_4)_2\text{F}_3$, it could also be that V^{3+} is oxidized to V^{4+} and it subsequently undergoes disproportionation. In our case, a 50%–50% V^{3+} – V^{4+} ordered composition was most likely formed upon Na^+ extraction toward Na_2VPF . Upon further oxidation, tetragonal symmetry suggests that only one site of V is present in the solid solution domain. When the final biphasic reaction takes place, either every vanadium has $3d^14s^0$ electronic structure (i.e., one unpaired electron) or they are distributed 50%–50% $3d^24s^0$ and $3d^04s^0$ (i.e., one vanadium with no unpaired electron and one with a pair). It seems in our case that this charge distribution is energetically favorable, especially in a system where the two vanadium environments share one corner. Table 3 gathers all the structural information related to NaVPF obtained from Rietveld refinement. V1–O distances are significantly shorter than V2–O ones and the V1–F3 bond

Table 3. Structural Parameters Obtained from Rietveld Refinement of in Situ Synchrotron Radiation Data for Fully Charged NaVPF, in the Space Group $Cmc2_1^a$

NaV ₂ (PO ₄) ₂ F ₃ (in situ)							
						$R_{\text{Bragg}} = 9.41\%$	
						$R_{\text{wp}} = 13.5\%$	
atoms	Wyckoff position	atomic position	x/a	y/b	z/c	occ	B_{iso}^b
V1	4a		1/2	0.248(4)	0.338(–)	1	0.63
V2	4a		0	0.251(3)	0.1908(7)	1	0.63
P ^c	8		0.244(2)	0.501(3)	0.276(1)	1	0.96
O1	8		0.357(5)	0.098(6)	0.368(3)	1	1.07
O2	8		0.347(7)	0.397(7)	0.361(3)	1	1.07
O3	8		0.157(7)	0.100(7)	0.193(3)	1	1.07
O4	8		0.163(5)	0.423(5)	0.170(2)	1	1.07
F(1)	4a		1/2	0.247(6)	0.520(6)	1	0.59
F(2)	4a		1/2	0.24(1)	0.875(2)	1	0.59
F(3)	4a		1/2	0.232(8)	0.187(3)	1	0.59
Na(2)	4a		1/2	0.071(2)	0.025(8)	0.88(9)	3.0

^aBecause of the floating origin of this space group, z/c of V1 is not refined. ^bRefined in the final stages of refinement and then fixed. ^cSoft constraints used on P–O distances (P–O = 1.54 Å ± 0.02 Å).

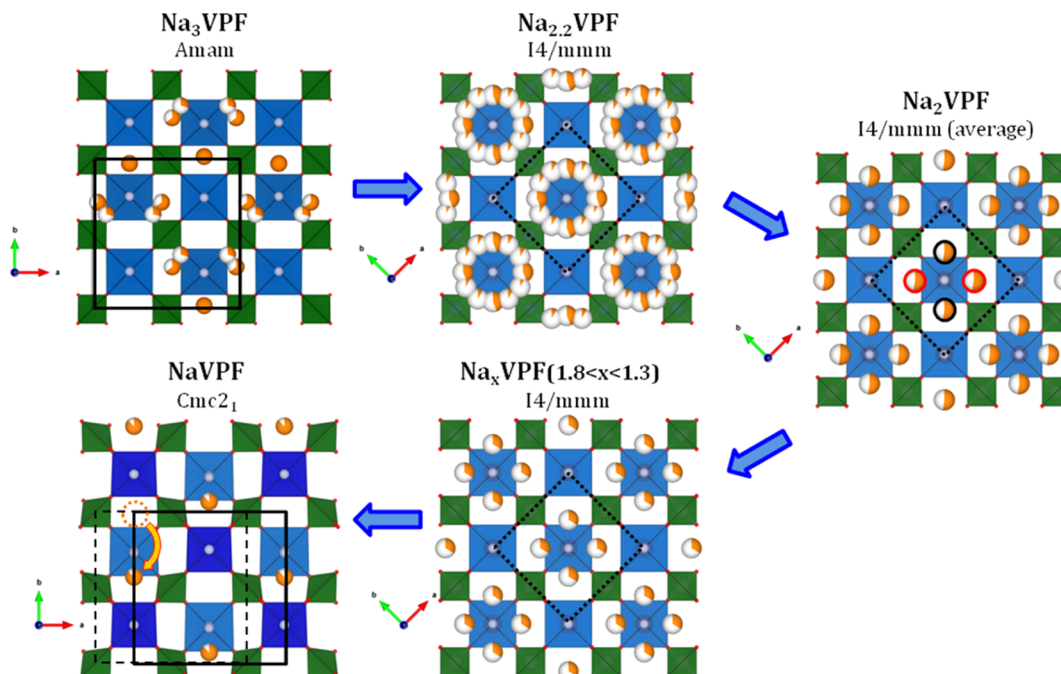


Figure 13. Sodium distribution obtained from Rietveld refinement of the different phases observed upon sodium extraction from Na₃VPF. Although a superstructure was observed for phase Na₂VPF, only the average structure was determined, thus the red/black circles indicate that only two positions out of four are expected to be occupied. For Na₁VPF, an orange dotted circle shows the second sodium site Na_{1A} which is filled in the structure of Na₃VPF (dashed cell), while it is now empty.

length is rather short (but already observed for other V⁵⁺–F containing compounds⁵⁶). Our conclusions on the V⁵⁺/V³⁺ disproportionation in NaVPF are based, noticeably, on structural refinements from in situ XRD data and will deserve supporting electronic structure calculations and oxidation-sensitive analysis techniques (XAS for example). Regarding sodium ions, we found them placed in a single fully occupied site Na_{1C}, partially corresponding to the Na_{1A} site of the pristine material. Its environment is a capped prism, composed of 4 oxygen and 3 fluorine atoms. Local charge compensation results in longer Na_{1C}–VI^{4.7+} bond length (3.48(3) Å) than

Na_{1C}–V^{2.3+} (3.35(3) Å). A strong difference is noticed with respect to Na₃VPF: in both cases the plane z = 0 hosts two Na₁ sites, but looking at the two arrangements (Figures 13) we notice that for NaVPF one of the two Na₁ positions is on the opposite side of the fluorine atom F1, with respect to the Na₃VPF case. This partially explains the need for a different space group (together with the fact that two V environments are present in NaVPF). To highlight the main crystal structure modifications observed upon sodium extraction from Na₃VPF, Figure 13 gives special emphasis to sodium rearrangement inside the unit cell. In light of this, the biphasic transition

between $\text{Na}_{1.3}\text{VPF}$ and NaVPF discussed above can be understood as follows: during the solid solution Na_xVPF ($1.8 \leq x \leq 1.3$) the vanadium polyhedral distortion increases significantly. At composition $\text{Na}_{1.3}\text{VPF}$, the sodium- and vanadium oxidation-disordered space group $I4/mmm$ is not energetically favorable anymore, and vanadium undergoes disproportionation. The $\sim 4^{-1}/4$ -filled sites stop being equivalent, and sodium ions converge on a single site in a bigger unit cell. This ordering happens on several small domains, underestimated by diffraction methods and separated by larger ones which remain disordered. Only when the ordered domains coalesce, diffraction is able to properly quantify them.

■ CONCLUSION

In this work we used high angular and intensity resolution synchrotron radiation diffraction to study the structural evolution of $\text{Na}_3\text{V}_2(\text{PO}_4)_2\text{F}_3$ in detail upon Na^+ extraction. The sodium deintercalation reaction, always reported to be a simple solid solution, reveals instead an extremely complicated phase transformations sequence. The two voltage domains around 3.7 and 4.2 V vs Na^+/Na have been analyzed separately. The lower voltage region never proceeds through a solid solution. Instead it reveals three biphasic reactions involving two intermediate phases, $\text{Na}_{2.4}\text{V}_2(\text{PO}_4)_2\text{F}_3$ and $\text{Na}_{2.2}\text{V}_2(\text{PO}_4)_2\text{F}_3$. The latter displays the same structure as the high-temperature form of $\text{Na}_3\text{V}_2(\text{PO}_4)_2\text{F}_3$, crystallizing in the tetragonal space group $I4/mmm$ due to Na^+ disordering. The former stabilizes instead an ordering on a longer range, up to a ~ 18 Å *d*-spacing, suggesting a superstructural arrangement. At the end of the first voltage–composition plateau, the phase $\text{Na}_2\text{V}_2(\text{PO}_4)_2\text{F}_3$ is obtained, revealing another possible superstructure due to sodium ordering and/or charge ordering. The higher voltage region shows a biphasic reaction upon which $\text{Na}_2\text{V}_2(\text{PO}_4)_2\text{F}_3$ disappears and subsequently a wide solid solution of compositions $\text{Na}_x\text{V}_2(\text{PO}_4)_2\text{F}_3$ ($1.8 \leq x \leq 1.3$), again sodium-disordered. Thanks to the high quality of these synchrotron data we could follow the reaction in detail and observe the structural modifications (e.g., cell parameters, bond lengths, polyhedral distortion, etc.) and sodium extraction (namely, sodium's site occupancy factor) in real time. The end-member $\text{NaV}_2(\text{PO}_4)_2\text{F}_3$ is finally attained through another biphasic reaction. The structure of this composition is different than those previously encountered, and a structural determination was carried out for the first time directly on data collected *operando*. It revealed a Cmc_2_1 space group, leading to a fully occupied sodium site and most importantly and unexpectedly to two different vanadium environments (a V^{3+} – V^{5+} couple in every biotahedron). The extremely small volume change observed from Na_3VPF to NaVPF , thus along the overall charge, further qualifies Na_3VPF as a material of choice for long-term cycling stability.

These *in situ* measurements demonstrate how obtaining good angular resolution and high intensity data is crucial because, delivering more detailed information, it can radically change the understanding of a given electrode's behavior. Our study proves how even resolving weak Bragg reflections can be a key element because it allows, for example, distinguishing among sodium ordered and sodium disordered structures. This is important as it paves the way to direct observation of fine reaction pathways and thus to a more exact knowledge of electrode materials' properties.

■ ASSOCIATED CONTENT

Supporting Information

Complementary experimental details, additional structural information, and electrochemical characterization. This material is available free of charge via the Internet at <http://pubs.acs.org/>.

■ AUTHOR INFORMATION

Corresponding Author

*(L. Croguennec) E-mail: crog@icmcb-bordeaux.cnrs.fr.

Notes

The authors declare no competing financial interest.

■ ACKNOWLEDGMENTS

Philippe Dagault (ICMAB), Alexis Saint-Georges (ICMAB and ICMCB), Alexandre Ponrouch (ICMAB), and Rosa Palacin (ICMAB) are acknowledged for help and discussion. This project was partly funded by the French National Research Agency ANR (Descartes program, Project SODIUM No. ANR-13-DESC-0001-02 and Investissements d'Avenir program, project STORE-EX No. ANR-10-LABX-76-01). Région Aquitaine is also acknowledged for financial support and the Institut Laue-Langevin for the Ph.D. thesis of M.B.

■ REFERENCES

- (1) Armand, M.; Tarascon, J. M. *Nature* **2008**, *451*, 652.
- (2) Tarascon, J.-M. *Nat. Chem.* **2010**, *2*, 510.
- (3) Wadia, C.; Albertus, P.; Srinivasan, V. *J. Power Sources* **2011**, *196*, 1593.
- (4) Palomares, V.; Serras, P.; Villaluenga, I.; Hueso, K. B.; Carretero-Gonzalez, J.; Rojo, T. *Energy Environ. Sci.* **2012**, *5*, 5884.
- (5) Braconnier, J. J.; Delmas, C.; Fouassier, C.; Hagenmuller, P. *Mater. Res. Bull.* **1980**, *15*, 1797.
- (6) Berthelot, R.; Carlier, D.; Delmas, C. *Nat. Mater.* **2011**, *10*, 74.
- (7) Moreau, P.; Guyomard, D.; Gaubicher, J.; Boucher, F. *Chem. Mater.* **2010**, *22*, 4126.
- (8) Boucher, F.; Gaubicher, J.; Cuisinier, M.; Guyomard, D.; Moreau, P. *J. Am. Chem. Soc.* **2014**, *136*, 9144.
- (9) Casas-Cabanas, M.; Roddatis, V. V.; Saurel, D.; Kubiak, P.; Carretero-Gonzalez, J.; Palomares, V.; Serras, P.; Rojo, T. *J. Mater. Chem.* **2012**, *22*, 17421.
- (10) Barker, J.; Saidi, M. Y.; Swoyer, J. L. *Electrochem. Solid-State Lett.* **2003**, *6*, A1.
- (11) Barker, J.; Saidi, M. Y.; Swoyer, J. L. *J. Electrochem. Soc.* **2004**, *151*, A1670.
- (12) Masquelier, C.; Croguennec, L. *Chem. Rev.* **2013**, *113*, 6552.
- (13) Jian, Z.; Zhao, L.; Pan, H.; Hu, Y.-S.; Li, H.; Chen, W.; Chen, L. *Electrochem. Commun.* **2012**, *14*, 86.
- (14) Saravanan, K.; Mason, C. W.; Rudola, A.; Wong, K. H.; Balaya, P. *Adv. Energy Mater.* **2013**, *3*, 444.
- (15) Zhu, C.; Song, K.; van Aken, P. A.; Maier, J.; Yu, Y. *Nano Lett.* **2014**, *14*, 2175.
- (16) Jian, Z.; Han, W.; Lu, X.; Yang, H.; Hu, Y.-S.; Zhou, J.; Zhou, Z.; Li, J.; Chen, W.; Chen, D.; Chen, L. *Adv. Energy Mater.* **2013**, *3*, 156.
- (17) Serras, P.; Palomares, V.; Goñi, A.; de Muro, I. G.; Kubiak, P.; Lezama, L.; Rojo, T. *J. Mater. Chem.* **2012**, *22*, 22301.
- (18) Serras, P.; Palomares, V.; Goñi, A.; Kubiak, P.; Rojo, T. *J. Power Sources* **2013**, *241*, S6.
- (19) Park, Y.-U.; Seo, D.-H.; Kim, B.; Hong, K.-P.; Kim, H.; Lee, S.; Shakoor, R. A.; Miyasaka, K.; Tarascon, J.-M.; Kang, K. *Sci. Rep.* **2012**, *2*, 704.
- (20) Park, Y.-U.; Seo, D.-H.; Kwon, H.-S.; Kim, B.; Kim, J.; Kim, H.; Kim, I.; Yoo, H.-I.; Kang, K. *J. Am. Chem. Soc.* **2013**, *135*, 13870.
- (21) Park, Y.-U.; Seo, D.-H.; Kim, H.; Kim, J.; Lee, S.; Kim, B.; Kang, K. *Adv. Funct. Mater.* **2014**, *24*, 4603.

- (22) Tsirlin, A. A.; Nath, R.; Abakumov, A. M.; Furukawa, Y.; Johnston, D. C.; Hemmida, M.; Krug von Nidda, H. A.; Loidl, A.; Geibel, C.; Rosner, H. *Phys. Rev. B* **2011**, *84*, 014429.
- (23) Barker, J.; Gover, R. K. B.; Burns, P.; Bryan, A. J. *J. Electrochem. Solid-State Lett.* **2006**, *9*, A190.
- (24) Gover, R. K. B.; Bryan, A.; Burns, P.; Barker, J. *Solid State Ionics* **2006**, *177*, 1495.
- (25) Barker, J.; Gover, R. K. B.; Burns, P.; Bryan, A. J. *J. Electrochem. Soc.* **2007**, *154*, A882.
- (26) Bianchini, M.; Brisset, N.; Fauth, F.; Weill, F.; Elkaim, E.; Suard, E.; Masquelier, C.; Croguennec, L. *Chem. Mater.* **2014**, *26*, 4238.
- (27) Park, Y.-U.; Seo, D.-H.; Kim, H.; Kim, J.; Lee, S.; Kim, B.; Kang, K. *Adv. Funct. Mater.* **2014**, n/a.
- (28) Ponrouch, A.; Dedryvere, R.; Monti, D.; Demet, A. E.; Ateba-Mba, J. M.; Croguennec, L.; Masquelier, C.; Johansson, P.; Palacin, M. *R. Energy Environ. Sci.* **2013**, *6*, 2361.
- (29) Xu, M.; Xiao, P.; Stauffer, S.; Song, J.; Henkelman, G.; Goodenough, J. B. *Chem. Mater.* **2014**, *26*, 3089.
- (30) Le Meins, J. M.; Crosnier-Lopez, M. P.; Hemon-Ribaud, A.; Courbion, G. *J. Solid State Chem.* **1999**, *148*, 260.
- (31) Shakoor, R.; Seo, D.-H.; Kim, H.; Park, Y.-U.; Kim, J.; Kim, S.-W.; Gwon, H.; Lee, S.; Kang, K. *J. Mater. Chem.* **2012**, *22*, 20535.
- (32) Chihara, K.; Kitajou, A.; Gocheva, I. D.; Okada, S.; Yamaki, J.-i. *J. Power Sources* **2013**, *227*, 80.
- (33) Liu, Z.; Hu, Y.-Y.; Dunstan, M. T.; Huo, H.; Hao, X.; Zou, H.; Zhong, G.; Yang, Y.; Grey, C. P. *Chem. Mater.* **2014**, *26*, 2513.
- (34) Song, W.; Cao, X.; Wu, Z.; Chen, J.; Zhu, Y.; Hou, H.; Lan, Q.; Ji, X. *Langmuir* **2014**, *30*, 12438.
- (35) Song, W.; Ji, X.; Wu, Z.; Yang, Y.; Zhou, Z.; Li, F.; Chen, Q.; Banks, C. E. *J. Power Sources* **2014**, *256*, 258.
- (36) Song, W.; Ji, X.; Chen, J.; Wu, Z.; Zhu, Y.; Ye, K.; Hou, H.; Jing, M.; Banks, C. E. *Phys. Chem. Chem. Phys.* **2015**, *17*, 159.
- (37) Serras, P.; Palomares, V.; Rojo, T.; Brand, H. E. A.; Sharma, N. J. *Mater. Chem. A* **2014**, *2*, 7766.
- (38) Sharma, N.; Serras, P.; Palomares, V.; Brand, H. E. A.; Alonso, J.; Kubiak, P.; Fdez-Gubieda, M. L.; Rojo, T. *Chem. Mater.* **2014**, *26*, 3391.
- (39) Meng, Y. S.; Hinuma, Y.; Ceder, G. *J. Chem. Phys.* **2008**, *128*, 104708.
- (40) Morcrette, M.; Chabre, Y.; Vaughan, G.; Amatucci, G.; Leriche, J. B.; Patoux, S.; Masquelier, C.; Tarascon, J. M. *Electrochim. Acta* **2002**, *47*, 3137.
- (41) Jumas, J.-C.; Sougrati, M.; Perea, A.; Aldon, L.; Olivier-Fourcade, J. *Hyperfine Interact.* **2013**, *217*, 107.
- (42) Liu, H.; Strobridge, F. C.; Borkiewicz, O. J.; Wiaderek, K. M.; Chapman, K. W.; Chupas, P. J.; Grey, C. P. *Science* **2014**, *344*, 1252817.
- (43) Gaubicher, J.; Boucher, F.; Moreau, P.; Cuisinier, M.; Soudan, P.; Elkaim, E.; Guyomard, D. *Electrochim. Commun.* **2014**, *38*, 104.
- (44) Fauth, F.; Peral, I.; Popescu, C.; Knapp, M. *Powder Diffr.* **2013**, *28*, S360.
- (45) Leriche, J. B.; Hamelet, S.; Shu, J.; Morcrette, M.; Masquelier, C.; Ouvrard, G.; Zerrouki, M.; Soudan, P.; Belin, S.; Elkaim, E.; Baudelet, F. *J. Electrochem. Soc.* **2010**, *157*, A606.
- (46) Ouvrard, G.; Zerrouki, M.; Soudan, P.; Lestriez, B.; Masquelier, C.; Morcrette, M.; Hamelet, S.; Belin, S.; Flank, A. M.; Baudelet, F. *J. Power Sources* **2013**, *229*, 16.
- (47) Barker, J.; Saidi, M. Y.; Swoyer, J. U.S. Patent 6,387,568, 2002.
- (48) Rietveld, H. M. *J. Appl. Crystallogr.* **1969**, *2*, 65.
- (49) Rodriguez-Carvajal, J. *Phys. B (Amsterdam, Neth.)* **1993**, *192*, 55.
- (50) Bianchini, M.; Ateba-Mba, J. M.; Dagault, P.; Bogdan, E.; Carlier, D.; Suard, E.; Masquelier, C.; Croguennec, L. *J. Mater. Chem. A* **2014**, *2*, 10182.
- (51) Ravnsbæk, D. B.; Xiang, K.; Xing, W.; Borkiewicz, O. J.; Wiaderek, K. M.; Gonet, P.; Chapman, K. W.; Chupas, P. J.; Chiang, Y. M. *Nano Lett.* **2014**, *14*, 1484.
- (52) Galceran, M.; Saurel, D.; Acebedo, B.; Roddatis, V. V.; Martin, E.; Rojo, T.; Casas-Cabanas, M. *Phys. Chem. Chem. Phys.* **2014**, *16*, 8837.
- (53) Zhang, X.; van Hulzen, M.; Singh, D. P.; Brownrigg, A.; Wright, J. P.; van Dijk, N. H.; Wagemaker, M. *Nano Lett.* **2014**, *14*, 2279.
- (54) Boucher, F.; Bourgeon, N.; Delb  , K.; Moreau, P.; Guyomard, D.; Ouvrard, G. *J. Phys. Chem. Solids* **2006**, *67*, 1238.
- (55) Serras, P.; Palomares, V.; Alonso, J.; Sharma, N.; del Amo, J. M. L.; Kubiak, P.; Fdez-Gubieda, M. L.; Rojo, T. *Chem. Mater.* **2013**, *25*, 4917.
- (56) Benkic, P.; Golic, L.; Koller, J.; Zemva, B. *Acta Chim. Slov.* **1999**, *46*, 239.

■ NOTE ADDED AFTER ASAP PUBLICATION

This article was published ASAP on April 7, 2015 with minor text errors in the Introduction section. The corrected version was published ASAP on April 9, 2015.